# Two-dimensional pentagonal CrX (X = S, Se or Te) monolayers: Antiferromagnetic semiconductors for spintronics and photocatalysts


| | |
|---|---|
| Journal: | *Physical Chemistry Chemical Physics* |
| Manuscript ID | CP-ART-04-2018-002470.R1 |
| Article Type: | Paper |
| Date Submitted by the Author: | 30-May-2018 |
| Complete List of Authors: | Chen, Wenzhou; Institute of Applied Physics and Materials Engineering, University of Macau,<br>Kawazoe, Yoshiyuki; Tohoku University, New Industry Creation Hatchery Center<br>Shi, Xingqiang; South University of Science and Technology of China, Physics<br>Pan, Hui; University of Macau, Faculty of Science and Technology |
| | |

# Two-dimensional pentagonal CrX (X = S, Se or Te) monolayers: Antiferromagnetic semiconductors for spintronics and photocatalysts

Wenzhou Chen[a], Yoshiyuki Kawazoe[b, c], Xingqiang Shi[*d] and Hui Pan[*a]

[a]Institute of Applied Physics and Materials Engineering, University of Macau, Macao SAR, P. R. China

[b]New Industry Creation Hatchery Center, Tohoku University, Sendai, Japan

[c]Department of Physics and Nanotechnology, SRM Institute of Science and Technology, Kattankulathur 603203, Tamil Nadu, India

[d]Department of Physics, Southern University of Science and Technology, Shenzhen 518055, China

* Corresponding Authors: huipan@umac.mo (H.P.); Tel: (853)88224427; Fax: (853)88222426; shixq@sustc.edu.cn (X. Q. S.)

**Abstract**

Two dimensional (2D) materials with *hexagonal* building blocks have received tremendous interests in the past years and show promising as nanoscale devices for versatile applications. Herein, we propose a new family of 2D *pentagonal* CrX (X = S, Se or Te) monolayers (penta-CrX) for their applications into electronics, spintronics and photocatalysis. We find that the 2D penta-CrX monolayers are thermally, structurally and mechanically stable. The penta-CrX monolayers are antiferromagnetic and semiconducting. We show that the magnetism is attributed to super-exchange induced by the ionic interactions among the Cr and X atoms and can be enhanced upon applying tension. We further show that the penta-CrS and penta-CrSe monolayers show good redox potentials versus normal hydrogen electrode, and their band gaps are comparable to the energy of photon in the visible light region, indicating their capable of maximal utilization of solar energy for water splitting. With intrinsic semiconducting and controllable magnetic properties, the proposed

penta-CrX monolayers may hold promising as flexible spintronics and photocatalysts.

## 1. Introduction

Spintronics have attracted extensive attention because of their unique properties of efficient data storage and transfer, and application in quantum computing.[1] It had been reported that spintronics can be realized in dilute-magnetic semiconductors and Heusler alloy.[2, 3] Recently, antiferromagnetic materials have been proposed to be more robust for spintronic and storage devices because they do not create parasitic magnetic fields, are insensitive to external magnetic field, and have a fast switching between antiferromagnetic states.[4] These antiferromagnetic materials can be metallic, semiconducting, and insulating.[4] Antiferromagnetic semiconductors are of particular interesting because of their intrinsic band gaps for applications into electronic devices.[4] Therefore, searching novel antiferromagnetic semiconductors for ultrafast spintronics are necessary.

Two-dimensional (2D) materials have been widely studied currently for their applications in various fields, such as nanodevices, optoelectronics, catalysis, and energy storage because of rich electronic, magnetic, and chemical properties.[5-11] Particularly, the applications of 2D nanomaterials in spintronics may lead to further enhancement of information transfer and storage. There are a plenty of magnetic 2D nanostructures, such as $Cr_2Ge_2Te_6$,[12] $CrI_3$,[13] CrOX (X = Cl or Br),[14] MXenes,[15-18] CrN,[19] defected $BC_3$,[20] $VX_2$,[21] $Mn_2C$,[22] $MoS_2$ nanoribbons,[23] strained $MoN_2$,[24] janus transition metal chalcogenides,[25] 1*T*-$CrX_2$,[26] and defected $PtSe_2$.[27] Unfortunately, most of them are ferromagnetic (FM) metals, FM semiconductors, and antiferromagnetic (AFM) metals. AFM semiconductors could only be achieved by functionalization and external tension previously,[16, 17] which made their applications complicated. Until most recently, there were only a few 2D AFM semiconductors reported, such as $CrCTe_3$ and $CrPS_4$.[28-30] Therefore, exploring pure AFM 2D intrinsic semiconductors is important to promote the practical applications. In this work, we designed a new family of monolayers, 2D pentagonal CrX (X = S, Se or Te) (penta-CrX) with

Cr-X-Cr three-atomic layer, for their applications in flexible spintronics based on the first-principles calculations. We demonstrate that penta-CrX are thermally, structurally, and mechanically stable. We find that penta-CrX monolayers hold intrinsic semiconducting and antiferromagnetic properties and show enhanced magnetic moments upon the application of moderate tensions. The band gaps of penta-CrS and penta-CrSe are tunable and comparable to the energy of photon in the visible light spectrum, which also promise them as photocatalysts for water splitting.

## 2. Computational methods

First-principles calculations were conducted within the density functional theory, as implemented in the Vienna Ab initio Simulation Package (VASP).[31] The interactions between the valence electrons and ionic cores were described by the projector augmented wave (PAW) method,[32] with valence electrons employed as $3d^5 4s^1$, $3s^2 3p^4$, $4s^2 4p^4$, and $5s^2 5p^4$ for Cr, S, Se, and Te respectively. The generalized gradient approximation (GGA) with the Perdew-Burke-Ernzerhof (PBE) functionals were employed to describe the correlation and exchange interactions.[33] The hybrid functionals (HSE06)[34] including the spin polarization were employed to calculate the magnetic properties and band structures, wherein a standard mixing fraction of 0.25 was adopted for the exact-exchange interaction. The effect of the spin-orbital coupling[35] on the band structure was also considered in our calculations. Gaussian smearing method was adopted to describe the electronic occupancies was described by the Gaussian smearing with a value of 0.05 eV. The electronic and ionic relaxations were terminated when the energy and force converge to within $1\times10^{-4}$ eV and 0.01 eV/Å, respectively. An energy cutoff of 550 eV and a k-points of 12×12×1 centered on the Gamma-point[36] were employed, which give a convergence of the total energy within 1 meV. The 2D monolayer was constructed by inserting a vacuum space of 18 Å along the z direction.

### 2.1 Phonon dispersion calculations

The calculations of phonon curves were performed by the finite displacement

approach[37] implemented in the PHONOPY code interfaced with VASP code.[38] A supercell with 72 atoms (3×3×1 unit cells) was employed to create the dynamic matrix and then compute the phonon curves.

## 3. Results and discussion

### 3.1 Crystal structures

Pentagonal 2D monolayers composed of pentagonal building blocks, such as penta-graphene,[39, 40] penta-$B_2C$,[41] and penta-TMB/C,[42] have been theoretically predicted. The existence of the pentagonal building blocks was recently confirmed experimentally for a 2D $PdSe_2$ layers.[43] In our work, the new 2D pentagonal monolayers, penta-CrX with an atomic ratio of 1:1, constitute three atomic layers in the sequence of X-Cr-X along the z direction (figure 1). The monolayers hold tetragonal symmetry and the unit cell contains four Cr atoms and four X atoms. Each Cr atom is five-fold coordinated with four X atoms and one Cr atom, while each X atom is four-fold coordinated with four Cr atoms. As a result, three Cr atoms and two X atoms form a buckled-pentagonal network with a thickness of $h_1$ (figure 1b). The structural parameters of the optimized penta-CrX, such as lattice constant (a) and effective thickness ($h_2$) of the unit cell, bond lengths ($b_1$ and $b_2$), bond angles ($\theta_1$, $\theta_2$, and $\theta_3$), and thickness of the buckled-pentagonal network are summarized in table 1. We see that the structural parameters, such as a, $b_2$, $\theta_3$, $h_1$ and $h_2$, increase from S→Se→Te, while the others, including $b_1$, $\theta_1$, $\theta_2$, decrease from S→Se→Te (table 1).

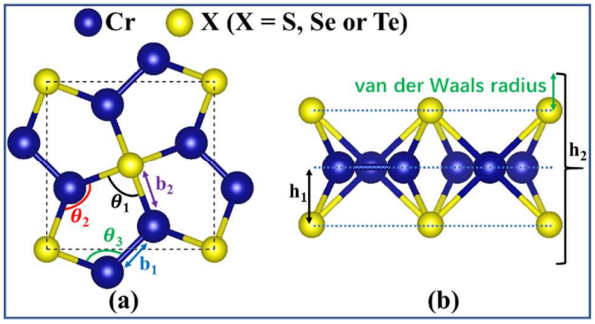


Figure 1 Top (a) and side (b) views of penta-CrX monolayers (X = S, Se or Te). The unit cell is indicated by black-dash lines in panel a. The blue and yellow spheres denote Cr and X (X = S, Se or Te) atoms, respectively. $b_1$ (bond length between Cr atoms); $b_2$ (bond length between Cr and X atoms); $\theta_1$ (angle between Cr-X-Cr); $\theta_2$ (angle between X-Cr-X); $\theta_3$ (angle

between X-Cr-Cr); $h_1$ (thickness of the buckled-pentagonal network); $h_2$ (vertical distance between the outermost S atoms plus their van der Waals radius).

Table 1 Structural parameters of the penta-CrX monolayers (X = S, Se or Te): lattice constant a; bond lengths $b_1$ and $b_2$; bond angles $\theta_1$, $\theta_2$, and $\theta_3$; thickness of the buckled-pentagonal network $h_1$; effective thickness of the unit cell $h_2$.

| Systems | a (Å) | $b_1$ (Å) | $b_2$ (Å) | $\theta_1$ ($^0$) | $\theta_2$ ($^0$) | $\theta_3$ ($^0$) | $h_1$ (Å) | $h_2$ (Å) |
|---|---|---|---|---|---|---|---|---|
| Penta-CrS | 4.92 | 2.12 | 2.40 | 67.1 | 93.3 | 106.9 | 1.50 | 6.59 |
| Penta-CrSe | 5.03 | 2.05 | 2.53 | 65.7 | 89.7 | 107.7 | 1.62 | 7.04 |
| Penta-CrTe | 5.25 | 2.03 | 2.71 | 64.3 | 86.5 | 108.3 | 1.79 | 7.69 |

**3.2 Dynamic, thermal, and mechanical stabilities.**

Before studying the physical properties of the penta-CrX monolayers, we firstly exam their stabilities. The phonon dispersion was calculated to investigate their dynamic stabilities. We see that there are no negative frequencies in the phonon dispersions of penta-CrS, penta-CrSe, and penta-CrTe monolayers (figure 2), indicating they are dynamically stable.

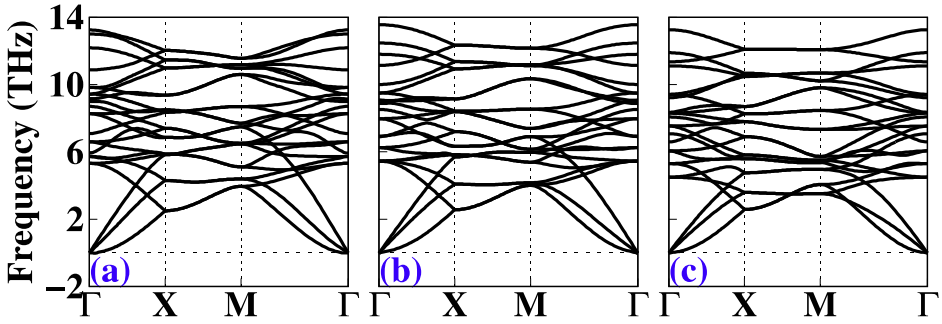


Figure 2 Calculated phonon dispersions of penta-CrS (a), penta-CrSe (b) and penta-CrTe (c).

The stabilities of the penta-CrX monolayers again thermal fluctuation were explored by the ab initio molecular dynamics (AIMD) simulations employing the canonical ensemble. The AIMD simulations are carried out for a supercell (3×3×1 unit cells) at 300 and 800 K for 3 ps with a time step of 1fs. We see that there is no structure reconstruction for the penta-CrX monolayers during the AIMD simulations (figures S1-S6), suggesting that the penta-CrX monolayers can survive up to 800 K.

The stabilities of the penta-CrX monolayers against mechanical strains were

investigated by calculating their elastic constants. For a mechanically stable material, the elastic constants should satisfy the following equations:[39] $C_{11}C_{22}-C_{12}^2 > 0$ and $C_{44} > 0$. Considering the tetragonal symmetry of penta-CrX, $C_{11} = C_{22}$, the criteria turn out to be $C_{11} > |C_{12}|$ and $C_{44} > 0$. The calculated $C_{11} > C_{12}$ and the $C_{44}$ is positive (table 2), suggesting that the penta-CrX monolayers are mechanically stable.

Table 2 Calculated elastic constants for penta-CrX (X = S, Se or Te) monolayers.

| Systems | $C_{11}$ (GPa) | $C_{12}$ (GPa) | $C_{44}$ (GPa) |
|---|---|---|---|
| Penta-CrS | 132 | 25 | 68 |
| Penta-CrSe | 119 | 33 | 60 |
| Penta-CrTe | 85 | 26 | 48 |

### 3.3 Electronic properties

We find that the penta-CrX monolayers are dynamically, thermodynamically, and mechanically stable. Consequently, their ground states are further investigated by considering spin-polarization. For this purpose, the energy differences $\Delta E_{NM-FM}$ (wherein $E_{NM}$ and $E_{FM}$ denote the energies of nonmagnetic and ferromagnetic states, respectively), and $\Delta E_{AFM-FM}$ (wherein $E_{AFM}$ is the energy of antiferromagnetic state) are calculated. Negative value of $\Delta E_{NM-FM}$ or $\Delta E_{AFM-FM}$ indicates the nonmagnetic or antiferromagnetic ground state, while positive value shows favorable ferromagnetic structure. As to the antiferromagnetic state, two configurations of spin-polarization are considered (figure S7). It is noted that the standard DFT usually show poor prediction for materials with localized electrons, which leads to underestimation of the electronic band gap, magnetic coupling and magnetic moments, partially due to inherent self-interaction errors. The hybrid-DFT (h-DFT) including the spin-polarization have shown better agreement with experiment, compared to standard DFT, for a wide range of materials and magnetic properties,[44, 45] and thus is employed in our work.

Table 3 Calculated energy differences ($\Delta E_{NM-FM}$, $\Delta E_{AFM1-FM}$, and $\Delta E_{AFM2-FM}$) for penta-CrX, and the magnetic moment of the Cr atom for the AFM2 magnetic ground state.

| Systems | $\Delta E_{NM-FM}$ (eV) | $\Delta E_{AFM1-FM}$ (eV) | $\Delta E_{AFM2-FM}$ (eV) | Moment $\mu_B$/(Cr atom) |
|---|---|---|---|---|

| | | | | |
|---|---|---|---|---|
| Penta-CrS | 0.4666 | 0.0022 | -0.6244 | ±2.913 |
| Penta-CrSe | 0.4390 | 0.0095 | -0.6152 | ±2.924 |
| Penta-CrTe | 0.2290 | -0.0048 | -0.3582 | ±3.019 |

We see that $\Delta E_{NM-FM}$ are positive, indicating FM are lower in energy than NM state. On the other hand, $\Delta E_{AFM2-FM}$ are negative, suggesting that AFM are lower in energy than FM state. We also find that the energy of AFM2 state is lower than that of AFM1 for the penta-CrX monolayers (table 3). Therefore, the ground states for the penta-CrX monolayers are antiferromagnetic with AFM2 spin configuration. The magnetic moments of the Cr atoms are ±2.913, ±2.924 and ±3.019 $\mu_B$ for penta-CrS, penta-CrSe, and penta-CrTe, respectively, while those of the S, Se or Te are zero, suggesting that the super-exchange is the plausible mechanism for the antiferromagnetic coupling.[46, 47] To determine the magnetic coupling, the exchange coupling parameters $J_1$ and $J_2$ (figure S8) were calculated by mapping the total energies of the penta-CrX with different spin-polarized states to the Ising model:[17, 22]

$$H= -\sum_{i,j} J_1 M_i \cdot M_j - \sum_{k,l} J_2 M_k \cdot M_l$$

where $J_1$ and $J_2$ are the nearest- and next-nearest-neighbors magnetic coupling parameters, and M is the local magnetic moment of the Cr atom. For the penta-CrX, each Cr atom is surrounded by one nearest and four next-nearest neighbor Cr atoms (figure S8). By mapping the h-DFT energies of the magnetic states to the Ising Hamiltonian, $J_1$ and $J_2$ can be expressed as following:

$$E_{FM} = -(J_1 + 4J_2) \cdot M_i^2$$

$$E_{AFM1} = -(J_1 - 4J_2) \cdot M_j^2$$

$$E_{AFM2} = J_1 \cdot M_k^2$$

where the values are about 1, ±1 and ±3 $\mu_B$ for $M_i$, $M_j$, and $M_k$, respectively. The magnetic coupling parameters $J_1/J_2$ are estimated to be -62.6/0.3 meV, -62.0/1.2 meV, and -35.6/-0.6 meV for penta-CrS, penta-CrSe and penta-CrTe, respectively. Negative and positive values of coupling parameters represent the antiparallel and parallel spin coupling, respectively. We see that $J_1$ are all negative for penta-CrX, indicating that the nearest-neighbor spins favor the antiparallel interactions and suggesting that the

AFM2 state are energetically more favorable than the FM and AFM1 states for all the penta-CrX. On the other hand, $J_2$ are positive for penta-CrS and penta-CrSe, while negative for penta-CrTe, suggesting that the FM states are lower in energy than the AFM1 states for penta-CrS and penta-CrSe, while the AFM1 state is energetically more favorable than the FM state for penta-CrTe, consisting with the results summarized in table 3.

Based on the ground states, their electronic structures were further investigated. The band structures of penta-CrX are calculated with and without SOC effects. We see that the SOC have no effects on the band structures of penta-CrS (figure 3a, blue lines) and penta-CrSe (figure 3b, blue lines). On the other hand, though the band structure of penta-CrTe show a small splitting along the Gamma-X and X-M paths (figure 3c, blue lines), the effect of SOC are found to be negligible on band-edge and thus the band gap of the penta-CrTe. Our calculations show that the penta-CrX systems are semiconductors with indirect band gaps, as indicated by the calculated band structures (figure 3) and densities of states (figure 4). Specifically, penta-CrS holds a band gap of 2.378 eV with the valence band maximum (VBM) at the k-point of (0.158, 0.158, 0) and the conduction band minimum (CBM) at (0.132, 0.132, 0). Penta-CrSe shows a band gap of 2.522 eV with its VBM at (0.158, 0.158, 0) and CBM at (0, 0, 0). Penta-CrTe presents a band gap of 1.298 eV with VBM at (0.447, 0.447, 0) and CBM at (0, 0, 0). The partial densities of states (PDOSs) show that the VBM and CBM of the penta-CrX are mainly attributed by the Cr-d states (figure 4). To confirm this, the band-decomposed partial densities were calculated for penta-CrS. We see that the band-decomposed charge densities for the highest valence band (figure 5a) and lowest conduction band (figure 5b) are accumulated on the Cr atoms, consistent with the calculated PDOSs (Figure 4a).

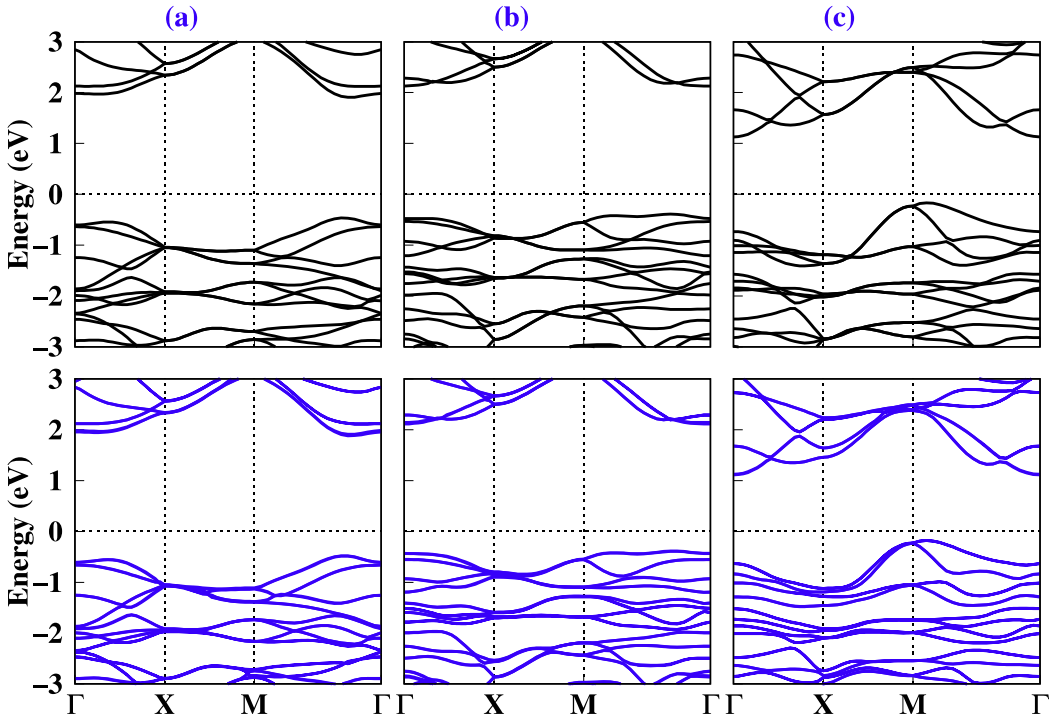


Figure 3 Calculated band structures of penta-CrS (a), penta-CrSe (b) and penta-CrTe (c) without SOC (black lines) and with SOC effects (blue lines).

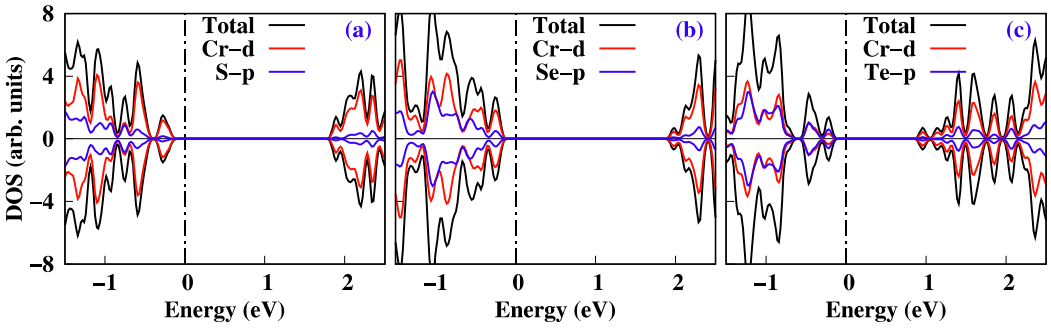


Figure 4 Calculated partial densities of states of penta-CrS (a), penta-CrSe (b) and penta-CrTe (c).

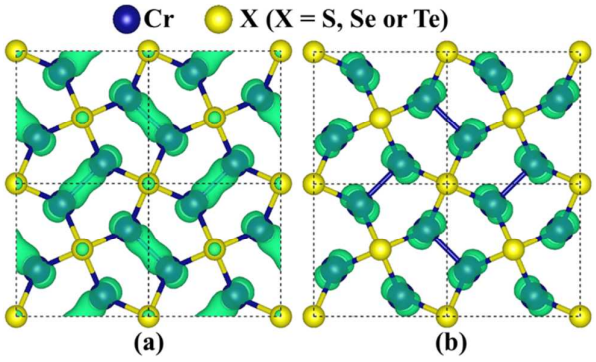

Figure 5 Calculated band-decomposed partial charge densities for the highest valence band (a) and lowest conduction band (b) for penta-CrS. The green color indicates the electron accumulation.

### 3.4 Effects of tensions on magnetism and band gap

We have shown that the penta-CrX monolayers are semiconducting with antiferromagnetic properties. To find their application in flexible devices, the effects of in-plane biaxial strains on their magnetism and band gap were investigated. The in-plane strain is defined as: $\varepsilon = (a-a_0)/a_0 \times 100\%$, where a and $a_0$ are the lattice constants of the strained and strain-free penta-CrX monolayers, respectively. Positive value of ε represents tension, while negative value is compression. The values of ε ranging from -3% to 3% were considered in our calculations. Upon the application of the strain, the ground states of the penta-CrX monolayers may differ from the strain-free condition. Therefore, we firstly studied the ground states of the penta-CrX monolayers under strain by calculating $\Delta E_{NM-FM}$ and $\Delta E_{AFM-FM}$ (figure 6). We see that $\Delta E_{AFM-FM}$ are negative (blue line-points in figure 6), while $\Delta E_{NM-FM}$ are positive (black line-points in figure 6) for penta-CrS, penta-CrSe and penta-CrTe in the whole considered ε, indicating that AFM states are lower in energies than the FM and NM states, and therefore are the ground states. Specifically, the $\Delta E_{AFM-FM}$ (negative) decreases upon tension, while increases with compression, which indicate the enhanced and reduced magnetism upon tension and compression, respectively.

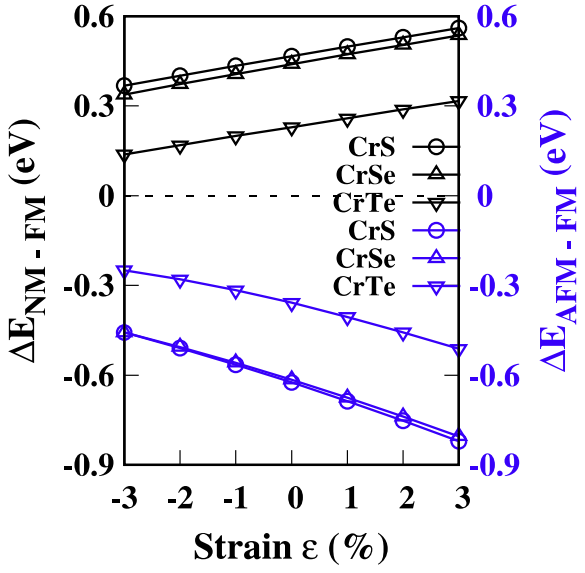

Figure 6 The $\Delta E_{NM-FM}$ and $\Delta E_{NM-FM}$ for the penta-CrX (X = S, Se, or Te) as a function of biaxial strains.

Our calculations show that the anti-ferromagnetism of the penta-CrX monolayer is robust against strain and enhanced as tension. The Bader charge calculations were performed to reveal the origin of the enhancement. We find that $M_{CrX}$ (the magnetic moment of the Cr atom) correlates strongly with CT (charge transfer from the Cr to X atoms) (figure 7). For example, $M_{CrS}$ increases from ±2.913 to ±3.254 $\mu_B$/atom as ε increases from 0% to 3%, and CT enhances accordingly from 0.851 to 0.895 electrons (figure 7a). On the other hand, $M_{CrS}$ decreases to ±2.689 at ε = -3%, while CT is reduced to 0.827 electrons. Similar trends are found for the penta-CrSe and penta-CrTe monolayers (figures 7b&c). Therefore, the enhancement is contributed to the improved super-exchanged due to increased charge transfer and increased magnetic moment.

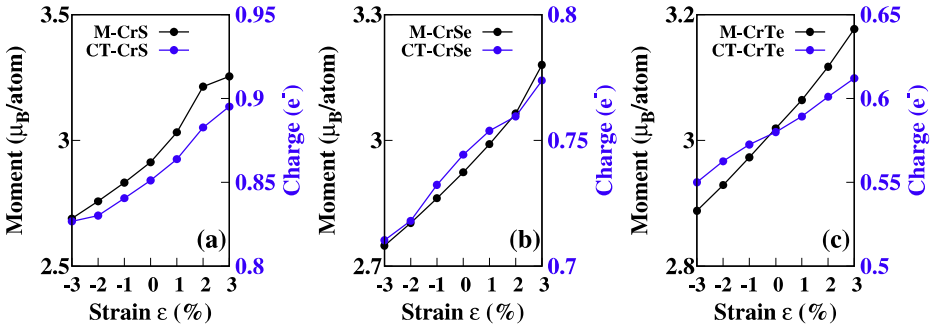


Figure 7 The $M_{CrX}$ (magnetic moment of the Cr atom) and CT (charge transfer from the Cr atoms to the X atoms) as a function of strain for penta-CrS (a), penta-CrSe (b) and penta-CrTe (c), respectively.

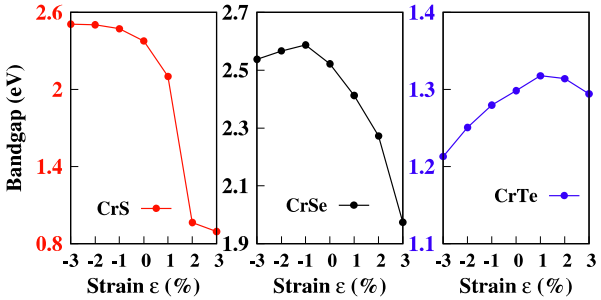


Figure 8 The evolution of the band gaps as a function of applying strains for the penta-CrX (X = S, Se or Te).

Besides the magnetic moments, the band gaps of the penta-CrX monolayers are also modulated by the applied strains (figure 8). We see the band gap of penta-CrS increases with compression, while decreases upon tension, with a minimum value of 0.894 eV at ε = 3% and a maximum value of 2.508 eV at ε = -3%. On the other hand, the band gap of penta-CrSe increases as ε increases from -3% to -1%, while decreases as ε further increases, with a maximum of 2.587 eV at ε = -1% and a minimum of 1.974 eV at ε = 3%. Penta-CrTe monolayer shows the same trend as penta-CrSe.

**3.5 Photocatalysts**

The semiconducting characteristic of the 2D penta-CrX monolayers with suitable band gaps to the energy of visible light may also suggest their applications in photocatalysis. To investigate their photocatalytic properties, we evaluated the redox ability of the penta-CrX by aligning their VBM and CBM with respect to the water oxidation/reduction potentials. The band-edge alignment with respect to the normal hydrogen electrode (NHE) are obtained by following equations:[48]

$$E_{CBM} = X - E_e - (1/2)E_g$$

$$E_{VBM} = E_{CBM} + E_g$$

where X represents the Mulliken electronegativity of the material, which is the geometric mean of the electronegativities of the constituent elements.[48, 49] X is 4.81, 4.68 and 4.52 eV for penta-CrS, penta-CrSe and penta-CrTe, respectively. $E_e$ denotes the energy of free electrons on the hydrogen scale (4.5 eV), and $E_g$ represents the band gap. For a suitable photocatalyst, its $E_{CBM}$ should be more negative than the reduction potential of $H^+/H_2$ (0 eV), while $E_{VBM}$ should be more positive than the oxidation potential of $O_2/H_2O$ (1.23 eV). We see that $E_{CBM}$ of penta-CrS, penta-CrSe and penta-CrTe monolayers within the considered ε, are more negative versus the reduction potential of $H^+/H_2$ (0 eV) (figure 9), suggesting their abilities to produce $H_2$ from water reduction. On the other hand, penta-CrS and penta-CrSe monolayers within most of the considered ε values are suitable for the production of $O_2$ from water because their $E_{CBM}$ values are more positive than the oxidation potential of $O_2/H_2O$ (1.23 eV), except penta-CrS when ε > 1% and penta-CrSe at ε = 3%.

Unfortunately, 2D penta-CrTe in the whole considered ε shows no ability to produce $O_2$ from water due to its less positive $E_{VBM}$ than the oxidation potential of $O_2/H_2O$ (1.23 eV).

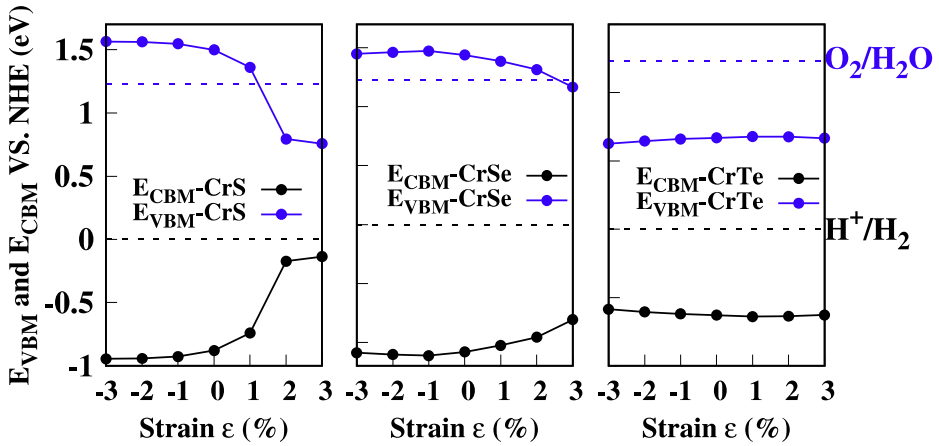


Figure 9 The calculated $E_{CBM}$ and $E_{VBM}$ of penta-CrS, penta-CrSe, and penta-CrTe monolayers with respect to normal hydrogen electrode (NHE) as a function of strains.

## 4. Conclusions

In summary, we present a new family of penta-CrX (X = S, Se or Te) monolayers based on the first-principles calculations. Their stability is confirmed by carrying out dynamic, thermal and mechanical calculations. The penta-CrX monolayers are antiferromagnetic and semiconducting. Importantly, the magnetism can be enhanced upon moderate tension due to the improved ionic interaction between Cr and X atoms. We further find that penta-CrS and penta-CrSe monolayers show excellent photocatalytic properties of maximal utilization of solar energy for water splitting, due to their optimal band gaps and suitable band alignment with the reduction potential of $H^+/H_2$ and more positive value of $E_{VBM}$ than the oxidation potential of $O_2/H_2O$. We expect that penta-CrX are promising for flexible spintronics and photocatalysts.

## 5. Acknowledgements

H. Pan acknowledges the University of Macau for financial support and the Science and Technology Development Fund from Macau SAR (FDCT-132/2014/A3)

and Multi-Year Research Grants (MYRG2015-00157-FST and MYRG2017-00027-FST) from Research & Development Office at University of Macau. X.Q. Shi acknowledges the financial support from the NSF of China (Grant Nos. 11474145, 11334003), the Shenzhen Fundamental Research Foundation (Grant No. JCYJ20170817105007999) and the special Program for Applied Research on Super Computation of the NSFC-Guangdong Joint Fund (the second phase) under Grant No. U1501501. One of the authors (YK) is thankful to the support by JSPS KAKENHI Grant Number 17H03384, HPCI System Research project (Project ID: hp170190), and ONRG Grant (Award Number of N62909-16-1-2036). The DFT calculations were performed at High Performance Computing Cluster (HPCC) of Information and Communication Technology Office (ICTO) at University of Macau.

## 6. References

1. T. Dietl and H. Ohno, *Rev. Mod. Phys.*, 2014, **86**, 187-251.
2. V. Alijani, J. Winterlik, G. H. Fecher, S. S. Naghavi and C. Felser, *Phys. Rev. B*, 2011, **83**, 184428-184434.
3. H. Pan, J. B. Yi, L. Shen, R. Q. Wu, J. H. Yang, J. Y. Lin, Y. P. Feng, J. Ding, L. H. Van and J. H. Yin, *Phys. Rev. Lett.*, 2007, **99**, 127201-127204.
4. V. Baltz, A. Manchon, M. Tsoi, T. Moriyama, T. Ono and Y. Tserkovnyak, *Rev. Mod. Phys.*, 2018, **90**, 015005-015060.
5. C. Tan, X. Cao, X.-J. Wu, Q. He, J. Yang, X. Zhang, J. Chen, W. Zhao, S. Han, G.-H. Nam, M. Sindoro and H. Zhang, *Chem. Rev.*, 2017, **117**, 6225-6331.
6. C. Si, Z. Sun and F. Liu, *Nanoscale*, 2016, **8**, 3207-3217.
7. Y. Shao, F. Zhang, X. Shi and H. Pan, *Phys. Chem. Chem. Phys.*, 2017, **19**, 28710-28717.
8. D. L. Duong, S. J. Yun and Y. H. Lee, *ACS Nano*, 2017, **11**, 11803-11830.
9. Y. Qu, H. Pan, C. T. Kwok and Z. Wang, *Phys. Chem. Chem. Phys.*, 2015, **17**, 24820-24825.
10. Y. P. Feng, L. Shen, M. Yang, A. Wang, M. Zeng, Q. Wu, S. Chintalapati and C.-R. Chang, *Compu. Mol. Sci.*, 2017, **7**, e1313-e1390.
11. T. T. Song, M. Yang, J. W. Chai, M. Callsen, J. Zhou, T. Yang, Z. Zhang, J. S. Pan, D. Z.

Chi, Y. P. Feng and S. J. Wang, *Sci. Rep.*, 2016, **6**, 29221-29229.

12. C. Gong, L. Li, Z. Li, H. Ji, A. Stern, Y. Xia, T. Cao, W. Bao, C. Wang, Y. Wang, Z. Q. Qiu, R. J. Cava, S. G. Louie, J. Xia and X. Zhang, *Nature*, 2017, **546**, 265-269.
13. B. Huang, G. Clark, E. Navarro-Moratalla, D. R. Klein, R. Cheng, K. L. Seyler, D. Zhong, E. Schmidgall, M. A. McGuire, D. H. Cobden, W. Yao, D. Xiao, P. Jarillo-Herrero and X. Xu, *Nature*, 2017, **546**, 270-273.
14. N. Miao, B. Xu, L. Zhu, J. Zhou and Z. Sun, *J. Am. Chem. Soc.*, 2018, **140**, 2417-2420.
15. H. Kumar, N. C. Frey, L. Dong, B. Anasori, Y. Gogotsi and V. B. Shenoy, *ACS Nano*, 2017, **11**, 7648-7655.
16. G. Gao, G. Ding, J. Li, K. Yao, M. Wu and M. Qian, *Nanoscale*, 2016, **8**, 8986-8994.
17. J. He, P. Lyu, L. Z. Sun, Á. Morales García and P. Nachtigall, *J. Mater. Chem. C*, 2016, **4**, 6500-6509.
18. G. Wang, *J. Phys. Chem. C*, 2016, **120**, 18850-18857.
19. A. V. Kuklin, A. A. Kuzubov, E. A. Kovaleva, N. S. Mikhaleva, F. N. Tomilin, H. Lee and P. V. Avramov, *Nanoscale*, 2017, **9**, 621-630.
20. Y. Ding, Y. Wang and J. Ni, *J. Phys. Chem. C*, 2010, **114**, 12416–12421.
21. H. Pan, *Sci. Rep.*, 2014, **4**, 7524-7531.
22. L. Hu, X. Wu and J. Yang, *Nanoscale*, 2016, **8**, 12939–12945
23. H. Pan and Y.-W. Zhang, *J. Phys. Chem. C*, 2012, **116**, 11752-11757.
24. Y. Wang, S. S. Wang, Y. Lu, J. Jiang and S. A. Yang, *Nano Lett.*, 2016, **16**, 4576-4582.
25. W. Chen, Y. Qu, L. Yao, X. Hou, X. Shi and H. Pan, *Journal of Materials Chemistry A*, 2018, DOI: 10.1039/C8TA01202D.
26. H. Y. Lv, W. J. Lu, D. F. Shao, Y. Liu and Y. P. Sun, *Phys. Rev. B*, **92**, 214419-214426.
27. M. Zulfiqar, Y. Zhao, G. Li, S. Nazir and J. Ni, *J. Phys. Chem. C*, 2016, **120**, 25030-25036.
28. S. Chabungbam and P. Sen, *Phys. Rev. B*, 2017, **96**, 045404-045413.
29. J. Lee, T. Y. Ko, J. H. Kim, H. Bark, B. Kang, S. G. Jung, T. Park, Z. Lee, S. Ryu and C. Lee, *ACS Nano*, 2017, **11**, 10935-10944.
30. Z. Z. Lin, *Phys. Chem. Chem. Phys.*, 2017, **19**, 3394-3404.
31. G. Kresse and J. Furthmüller, *Phys. Rev. B*, 1996, **54**, 11169-11186.
32. P. E. Blöchl, *Phys. Rev. B*, 1994, **50**, 17953-17979.

33. J. P. Perdew, K. Burke and M. Ernzerhof, *Phys. Rev. Lett.*, 1996, **77**, 3865-3868.
34. J. Heyd, G. E. Scuseria and M. Ernzerhof, *J. Chem. Phys.*, 2003, **118**, 8207-8215.
35. D. Hobbs, G. Kresse and J. Hafner, *Phys. Rev. B*, 2000, **62**, 11556-11570.
36. H. J. Monkhorst and J. D. Pack, *Phys. Rev. B*, 1976, **13**, 5188-5192.
37. K. Parlinski, Z. Q. Li and Y. Kawazoe, *Phys. Rev. Lett.*, 1997, **78**, 4063-4066.
38. A. Togo and I. Tanaka, *Scripta Mater.*, 2015, **108**, 1-5.
39. Shunhong Zhang, Jian Zhou, Qian Wang, Xiaoshuang Chen, Yoshiyuki Kawazoe and P. Jena, *PNAS*, 2015, **112**, 2372–2377.
40. H. Sun, S. Mukherjee and C. V. Singh, *Phys. Chem. Chem. Phys.*, 2016, **18**, 26736-26742.
41. F. Li, K. Tu, H. Zhang and Z. Chen, *Phys. Chem. Chem. Phys.*, 2015, **17**, 24151-24156.
42. Y. Shao, M. Shao, Y. Kawazoe, X. Shi and H. Pan, *Journal of Materials Chemistry A*, 2018, DOI: 10.1039/C8TA00635K.
43. A. D. Oyedele, S. Yang, L. Liang, A. A. Puretzky, K. Wang, J. Zhang, P. Yu, P. R. Pudasaini, A. W. Ghosh, Z. Liu, C. M. Rouleau, B. G. Sumpter, M. F. Chisholm, W. Zhou, P. D. Rack, D. B. Geohegan and K. Xiao, *J. Am. Chem. Soc.*, 2017, **139**, 14090-14097.
44. C. Franchini, V. Bayer, R. Podloucky, J. Paier and G. Kresse, *Phys. Rev. B*, 2005, **72**, 045132-045137.
45. C. Franchini, R. Podloucky, J. Paier, M. Marsman and G. Kresse, *Phys. Rev. B*, 2007, **75**, 195128-195138.
46. P. W. Anderson, *Phys. Rev.*, 1950, **79**, 350-356.
47. W. Chen, H.-F. Li, X. Shi and H. Pan, *J. Phys. Chem. C*, 2017, **121**, 25729-25735.
48. Y. K. Lim, E. W. Keong Koh, Y.-W. Zhang and H. Pan, *J. Power Sources*, 2013, **232**, 323-331.
49. R. G. Parr and R. G. Pearson, *J. Am. Chem. Soc.*, 1983, **105**, 7512-7516.